CHEMISTRY OF MATERIALS

Mn-Induced Stabilization of a β-Alumina-Type Defect Structure in Barium Hexaferrite Nanoplatelets

Darko Makovec,* Matic Poberžnik, Janvit Teržan, Tomaž Mertelj, Damjan Vengust, Goran Dražić, Darja Lisjak, and Sašo Gyergyek

Cite This: https://doi.org/10.1021/acs.chemmater.6c00103 Read Online

ACCESS | Metrics & More | Article Recommendations | Supporting Information

ABSTRACT: Hexaferrite nanoplatelets exhibit size-dependent structural variations influencing their magnetic properties. Here, we synthesized Mn-substituted barium ferrite nanoplatelets via hydrothermal methods, achieving up to ~27% Fe substitution. Advanced STEM and Raman analyses revealed depletion of Fe(2b) trigonal lattice sites and associated oxygen vacancies, forming a β-alumina-type ferrite structure—representing the first pure Ba^{2+} β-ferrite analogue. First-principles modeling confirmed the thermodynamic stabilization of this defected structure at higher Mn/Fe ratios. Mn substitution reduced nanoplatelet size and suppressed magnetic properties, which were restored upon annealing at 800 °C, reverting to the M-type hexaferrite structure with expected magnetic behavior. These findings elucidate nanoscale structural adaptations induced by chemical substitution and offer insights into tailoring the magnetic properties of barium ferrite nanoplatelets through controlled synthesis and post-treatment.

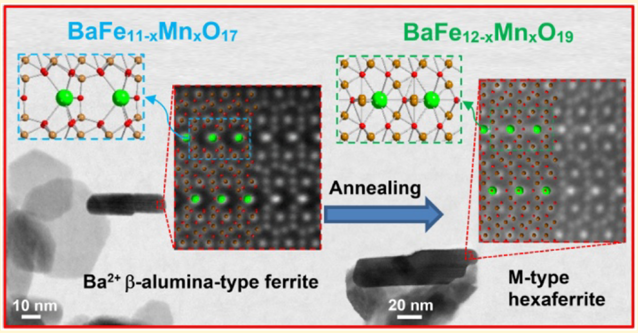

■ INTRODUCTION

The structure—and consequently the composition—of inorganic materials can change significantly when they are synthesized in the form of nanoparticles.[1] These changes arise from two thermodynamically driven phenomena: (i) the crystal structure adapts to the restricted size and high surface-to-volume ratio of the nanoparticles, and (ii) metastable structural polymorphs, which form during synthesis due to their lower nucleation barriers compared to the equilibrium phase (i.e., the Ostwald step rule),[2] can be stabilized at the nanoscale.[1] These two effects are important not only for understanding the properties of nanomaterials but also represent a promising strategy for discovering new nanomaterials.

The adaptation of crystal structures to confined nanoscale dimensions is especially pronounced in inorganic materials with complex structures and compositions, such as mixed oxides composed of alternating layers of several structural blocks.[3−5] Hexagonal ferrites, or hexaferrites, possess structures built from three types of blocks: a cubic S block, a hexagonal R block, and a hexagonal T block. M-type hexaferrite ($AFe_{12}O_{19}$, where A denotes a large divalent ion such as Ba^{2+}, Sr^{2+}, or Pb^{2+}) is the simplest member of the hexaferrite family, consisting solely of alternating hexagonal R $(AFe_6O_{11})^{2-}$ and cubic S $(Fe_6O_8)^{2+}$ structural blocks. The unit cell (space group $P6_3/mmc$, $a = 0.59$ nm, $c = 2.3$ nm) can be described by the RSR*S* stacking sequence, where the asterisk indicates a 180° rotation of the block around the hexagonal c-axis. The A^{2+} ions are located in the center of the R block, while Fe^{3+} ions occupy five distinct crystallographic sites: one tetrahedral ($4f_1$), three octahedral (12k, 2a, $4f_2$), and one trigonal bipyramidal (2b) (Figure 1a). The magnetic moments of the Fe^{3+} ions at the 12k, 2b, and 2a sites are aligned parallel to the c-axis, whereas those at the $4f_1$ and $4f_2$ sites are aligned antiparallel to the c-axis, resulting in a net magnetic moment of 40 μ_B (see Figure 11a).[6,7] M-type hexaferrites also exhibit high uniaxial magnetocrystalline anisotropy ($K_1 = 3.3 \times 10^4$ J/m^3), with the easy axis oriented parallel to the hexagonal c-axis.[6,7]

In the form of nanoparticles, hexaferrites adopt the shape of hexagonal nanoplatelets (NPLs), which possess a specific structure and composition defined by the termination of their basal surfaces with Fe-only S structural blocks.[4,8] Owing to this distinct structure and composition, they can be regarded as structural variations of hexaferrites stabilized at the nanoscale.[9] During hydrothermal synthesis, barium hexaferrite (BHF) nucleates as ultrafine primary NPLs (up to 20 nm wide and less than 2 nm thick) with a structure consisting of a single R structural block sandwiched between two S blocks. The SRS* stacking sequence represents the smallest entity exhibiting the

Received: January 14, 2026
Revised: February 19, 2026
Accepted: March 4, 2026

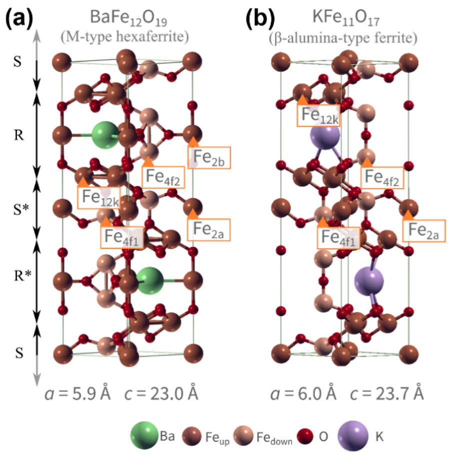

Figure 1. Schematic representations of the unit cells of the M-type hexaferrite structure (a) and the β-alumina-type ferrite structure (b). In the M-type hexaferrite, the positions of the five distinct Fe sites are indicated: tetrahedral ($4f_1$), octahedral (12k, 2a, $4f_2$), and trigonal (2b). The site notation in the β-alumina-type ferrite is given by analogy with the M-type structure; notably, this structure lacks the trigonal (2b) Fe sites and contains four fewer oxygen ions per unit cell.

hexaferrite motif. The subsequent thickening of NPLs proceeds in a discrete, step-like manner through the addition of RS segments to the initial SRS* structure. The addition of just one RS segment to the weakly magnetic SRS* structure (yielding the SRS*R*S structure, Figure 1) results in hard-magnetic properties characteristic of M-hexaferrites. Due to the termination of structure with the Fe-only S structural blocks the NPLs exhibit a Fe-rich composition when compared to the bulk.[4,9]

In contrast, strontium hexaferrite nucleates as ultrafine NPLs with a structure distinct from that of M-hexaferrite. This phase remains stable in the form of fine NPLs but transforms into the hexaferrite structure upon further growth, without any change in composition.[5] This observation clearly indicates that the phase is a metastable polymorph of hexaferrite stabilized at the nanoscale.

Apart from the adaptation of crystalline structure to the nanoscale, chemical substitution can have entirely different—even opposite—effects on the properties of nanoparticles compared to the bulk.[10] For example, partial substitution of Fe with Sc in BHF NPLs significantly increases their saturation magnetization (M_S), even though Sc substitution is known to greatly decrease the M_S of bulk BHF.[10,11]

In this work, we report remarkable changes in the structure and magnetic properties of Mn-substituted barium ferrite NPLs synthesized via a hydrothermal method. Mn substitution leads to depletion of the Fe(2b) lattice sites in M-type hexaferrite, which, in the extreme case, results in the formation of a β-alumina-type ferrite structure—reported here for the first time in the Ba^{2+} analogue. The β-ferrite structure typically forms with alkali ions (e.g., $K^+Fe_{11}O_{17}$; see Figure 1b). These compounds are antiferromagnetic and are primarily valued as ionic and electronic conductors, with applications as electrode materials in batteries and sensors.[12−14]

In bulk BHF, a large proportion of Fe can be substituted by Mn, with compositions with x exceeding 9 in the $BaFe_{12-x}Mn_xO_{19}$ formula. However, at $x > 8$, the crystal symmetry changes from hexagonal to triclinic as a consequence of the Jahn−Teller effect.[15,16] Mn ions occupy all Fe sites except the trigonal 2b sites.[17−19] Within the hexaferrite structure, Mn is incorporated in mixed oxidation states; Mn^{3+} undergoes disproportionation into Mn^{2+} and Mn^{4+}. Specifically, incorporation of Mn^{2+} at the tetrahedral $4f_1$ sites is compensated by Mn^{4+} at the octahedral sites.[16,17,19] Incorporation of high Mn concentrations disrupts the collinear ferrimagnetic ordering in the 2a and 12k octahedral sublattices and significantly reduces the saturation magnetization.[17]

Hexaferrite ceramics are among the earliest commercialized magnet materials (introduced by Philips in the early 1950s).[6] Recently, they have regained significant scientific and technological interest in response to the growing demand for rare-earth-free magnets driven by current geopolitical challenges. Hexaferrites remain the most widely used permanent magnets worldwide (by weight) and are employed in magnetic recording, as well as in microwave devices and absorbers.[7] More recently, they have also attracted attention for their magnetoelectric properties.[20]

Current research on ferrites has increasingly focused on NPLs. Their remarkable magnetic properties—dominated by the orientation of magnetic moments perpendicular to the basal planes, combined with their platelet-like morphology and colloidal stability in various liquid media[21]—have already enabled the development of new smart multifunctional hybrid materials. These include the first liquids exhibiting spontaneous magnetic ordering (ferromagnetic fluids),[22−26] the first multiferroic liquids exhibiting both ferroelectric and ferromagnetic ordering,[27] magneto-optical suspensions[28−31] and composites,[32] sensors,[30,31,33,34] novel spin-memory devices,[35,36] and self-biased nonreciprocal devices.[37] In addition, hexaferrite NPLs have been explored for magneto-mechanical cancer cell destruction[38] and diagnostic imaging.[39]

EXPERIMENTAL SECTION

A 200 mL aqueous solution containing 6.59 mmol of barium(II) nitrate, 19.76 mmol of iron(III) nitrate, and manganese(II) nitrate with an Mn/Fe ratio ranging from 0 to 1.4 was rapidly mixed with 200 mL of an aqueous solution containing 1.13 mol NaOH (the materials used are listed in the Supporting Information, SI). Note that barium was added in large excess ((Fe + Mn)/Ba ratio = 5), considering the stoichiometry of $BaFe_{12-x}Mn_xO_{19}$ formation.[40] The mixture was then sealed in a 1000 mL Inconel autoclave vessel (Model 4522 M, Parr Instrument Co.) and heated at a rate of 3 °C/min to 250 °C. The autoclave was then switched off, and the temperature began to decrease after approximately 10 min.

Upon cooling, the product was thoroughly washed with diluted nitric acid to dissolve any Ba-rich compounds formed as a result of the barium excess. The NPLs were subsequently washed three times with distilled water, with intermediate sedimentation performed by ultracentrifugation (Thermo Scientific Sorvall Lynx 600), and finally dried at 60 °C in ambient air. To simplify sample designation, the products were labeled as "BFM-X," where X represents the Mn/Fe atomic ratio in the starting composition.

The NPLs were also annealed in air for 2 h at 800 and 1000 °C.

The NPLs were characterized by transmission electron microscopy (TEM, JEOL 2100), aberration-corrected scanning transmission electron microscopy (STEM, JEOL ARM 200CF operated at 80 kV and Thermo Fisher Scientific Spectra 300 operated at 200 kV), X-ray diffractometry (XRD, PANalytical X'Pert PRO) X-ray photoelectron spectroscopy (XPS, PHI VersaProbe 3 AD), and Raman spectrometry (NTMDT Spectrum Instruments NTEGRA), thermogravimetric analysis and differential thermal analysis (TGA)/DTA, Netzsch Jupiter 449 C), and Fourier-transform infrared spectroscopy in attenuated total reflectance mode (FTIR−ATR, Shimadzu IRSpirit spectrometer). Magnetic properties were measured at room temperature using a vibrating sample magnetometer (VSM, Lake Shore 7307). To avoid issues arising from the unknown preferential orientation of the highly anisotropic nanoplatelets within the sample, the NPLs were mixed with sucrose, pressed into cubic compacts, and measured by averaging the results in three orthogonal directions. Further details of the characterization methods are provided in the SI.

■ COMPUTATIONAL DETAILS

The calculations were performed within the framework of Density Functional Theory (DFT). Specifically, the Perdew-Burke-Ernzerhof (PBE) functional[41] in combination with a plane-wave basis set and norm conserving pseudopotentials.[42] The plane-wave cutoff was set to 90 Ry for all calculations. The Brillouin zone was integrated with a 4 × 4 × 1 Monkhorst–Pack grid.[43] Since BHF is known to be ferrimagnetic, spin-polarization was considered and we set the starting magnetization as predicted by Gorter for this material.[44] The magnetization of the substituting Mn ions was also set according to the Fe ion it replaces in the structure. To account for the electron localization in highly correlated materials we employ the DFT+U formalism,[45] where the U parameter was computed self-consistently[46] for bulk BHF. We obtained an average U parameter of 4.1 eV for electrons in the 3d shell of Fe, whereas for sake of simplicity this parameter was set to the same value of 4.1 for the 3d electrons of Mn. Employing this methodology, the volume cell minimization of the BHF bulk hexagonal unit-cell resulted in optimized lattice parameters of a = 0.60 nm and c = 2.35 nm. The structure of the unit cell, iron sublattices and their spin orientations are summarized in Figure 1. All calculations were performed with the Quantum ESPRESSO suite for electronic structure calculations[47,48] whereas the molecular graphics were produced by the XCRYSDEN graphical package.[49]

We define the iron vacancy formation energy (ΔE_{vac}) as in bulk BHF

$$\Delta E_{\text{vac}} = E_{\text{bulk+vac}} + N_{\text{vac}} E^{\text{Fe}}{}_{\text{bulk}} - E^{\text{BHF}}{}_{\text{bulk}} \tag{1}$$

where $E_{\text{bulk+vac}}$ is the DFT total energy of the BHF unit cell containing N_{vac} vacancies, $E^{\text{Fe}}{}_{\text{bulk}}$ is the total energy per iron atom in iron bulk and $E^{\text{BHF}}{}_{\text{bulk}}$ is the total energy of the bulk BHF unit cell. Further, we define the Mn substitution energy as

$$\Delta E_{\text{subs}} = E_{\text{subs}} + N_{\text{subs}} E^{\text{Fe}}{}_{\text{bulk}} - E^{\text{BHF}}{}_{\text{bulk}} - N_{\text{subs}} E^{\text{Mn}}{}_{\text{bulk}} \tag{2}$$

where E_{subs} is the total energy of the unit cell where N_{subs} iron ions have been substituted by the same number of Mn ions, $E^{\text{Mn}}{}_{\text{bulk}}$ is the total energy per atom of Mn bulk and $\text{E}^{\text{BHF}}{}_{\text{bulk}}$ is the total energy of the unit cell of pristine BHF.

To provide a more comprehensive picture of the relative thermodynamic stability of the structures considered with DFT calculations we also employed atomistic thermodynamics.[50] Specifically, we consider the reaction:

$$\text{BaFe}_{12}\text{O}_{19} + x\text{Mn} \rightarrow \text{BaFe}_{12-y}\text{Mn}_y\text{O}_{19-z} + y\text{Fe} + z/2\text{O}_2 \tag{3}$$

where x is the number of Mn atoms that replace Fe atoms in bulk BHF, y is the number of Fe ions that are removed (either by Mn-substitution, vacancy formation or both), and z is the number of the oxygen ions that are removed from the structure. We define the Gibbs energy for this process as

$$\Delta G = g_{\text{subs+vac}} + y\mu_{\text{Fe}} + z\mu_{\text{O}} - g_{\text{BHF}} + x\mu_{\text{Mn}} \tag{4}$$

where $g_{\text{subs+vac}}$ and g_{BHF} are approximated as the DFT+U total energies of the Mn-substituted (and vacancy containing) bulk unit cell and the pristine BHF bulk unit cells, respectively. The terms μ_{Fe}, μ_{O} and μ_{Mn} represent the chemical potentials of iron, oxygen, and manganese, respectively. We approximate the oxygen chemical potential as the DFT total energy of the oxygen molecule along with the thermal contributions to energy and entropy at standard conditions (p_0 = 1 atm, T_0 = 298 K). Iron and manganese chemical potentials are defined with respect to their bulk values, i.e, $\mu_{\text{Fe}} = \mu_{\text{Fe}}{}^{\text{bulk}} + \Delta\mu_{\text{Fe}}$ and $\mu_{\text{Mn}} = \mu_{\text{Mn}}{}^{\text{bulk}} + \Delta\mu_{\text{Mn}}$, where $\mu_{\text{Fe}}{}^{\text{bulk}}$ and $\mu_{\text{Mn}}{}^{\text{bulk}}$ are approximated as the DFT total energies per atom in iron and manganese bulk, respectively.

■ RESULTS

Properties of Mn-Substituted Barium Ferrite NPLs

XRD characterization of the hydrothermally synthesized samples with Mn addition showed diffraction patterns characteristic of hexaferrite NPLs, even at the highest Mn/Fe ratio of 1.4 (Figure 2). The diffraction pattern of the NPLs differs significantly from that of bulk BHF. Owing to the very small dimension of the NPLs along the c-axis of their hexagonal structure—which reflects their reduced thickness—the (hkl) peaks with l ≠ 0 are very broad or even absent for low l values. In addition, the relative peak intensities are altered due to the presence of preferential orientation.[51] Only at the highest Mn/Fe ratio of 1.4 were additional peaks corresponding to secondary phases observed alongside the NPL peaks. These secondary peaks were assigned to Mn-rich $\text{BaMn}_{1-x}\text{Fe}_x\text{O}_{3-\delta}$ hexagonal perovskite (PDF card No. 04-0023-4771)[52] and to BaMn_3O_6 (PDF card No. 04-0011-6449).[53] The observed peak positions for the both secondary phases were shifted significantly compared with the reference, suggesting compositional deviations from the standards.

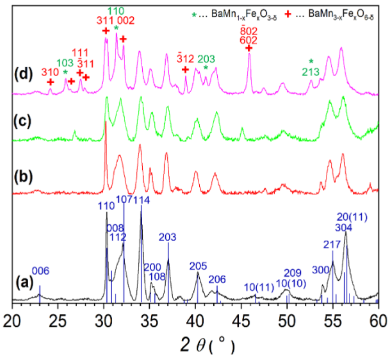

Figure 2. XRD patterns of samples hydrothermally synthesized with different Mn/Fe ratio: BFM-0 (a), BFM-0.043 (b), BFM-0.33 (c), and BFM-1.4 (d). Colored indexing symbols above the reflections indicate different phases: blue indices correspond to barium hexaferrite (PDF card No. 04-0023-4771); green indices correspond to the hexagonal perovskite $\text{BaMn}_{1-x}\text{Fe}_x\text{O}_{3-\delta}$ (PDF card No. 04-0023-4771); red indices correspond to BaMn_3O_6 (PDF card No. 04-0011-6449).

As shown in our previous research, during hydrothermal synthesis unsubstituted BHF forms below 100 °C as ultrafine primary NPLs of discoid shape, less than 20 nm in width.[4,51] The thickness of these initial NPLs is fixed at ∼1.6 nm by their specific structure, which can be represented as an SRS* sequence of the M-hexaferrite SRS*R* unit cell.[4] The final hexagonal platelet shape, with side surfaces parallel to the {1010} prismatic planes, develops during Ostwald ripening above approximately 150 °C. In this process, individual primary NPLs grow at the expense of others; their lateral dimensions increase substantially, while their thickness grows more slowly in a stepwise manner, through the addition of SR segments to the initial SRS* structure.[4]

TEM images of the samples hydrothermally synthesized at 250 °C with increasing Mn content are shown in Figure 3. The unsubstituted barium ferrite NPLs underwent Ostwald ripening and reached widths of ∼100−800 nm and thicknesses of ∼10 nm (Figure 3a). The addition of Mn had a profound effect on NPL growth. The BFM-0.043 sample, synthesized with the lowest Mn content, exhibited a bimodal size distribution consisting of smaller primary NPLs (∼7−15 nm wide) and larger NPLs (∼50−300 nm wide and ∼5−7 nm thick) (Figure 3b). In unsubstituted hexaferrites, such a bimodal size distribution is typically observed shortly after the onset of Ostwald ripening at ∼150 °C.[4]

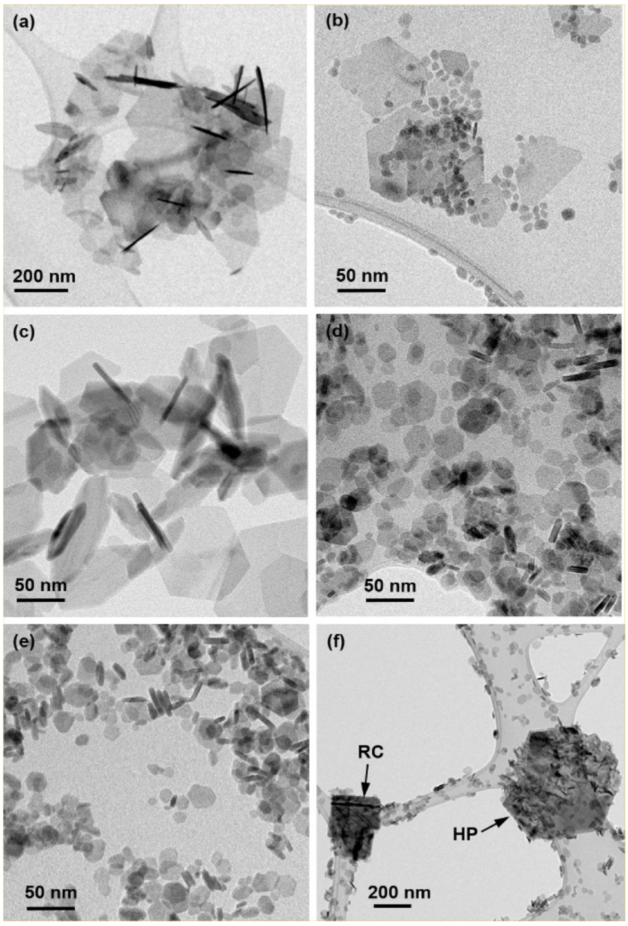

Figure 3. TEM images of samples BFM-0 (a), BFM-0.043 (b), BFM-0.14 (c), BFM-0.33 (d), and BFM-1.4 (e, f) hydrothermally synthesized by heating the autoclave to 250 °C ("RC"··· elongated rectangular crystals correspond to Fe-substituted $BaMn_3O_6$, "HP"··· hexagonal platelets correspond to the hexagonal perovskite $BaMn_{1-x}Fe_xO_{3-\delta}$).

Further increasing of the Mn/Fe ratio led to more uniform NPLs. In the BFM-0.14 sample, the NPLs were ∼30−150 nm wide (Figure 3c), while in the BFM-0.33 sample they were only ∼10−50 nm wide (Figure 3d). With additional increases in the Mn/Fe ratio, the lateral dimensions of the NPLs remained nearly unchanged (Figure 3e and f). Interestingly, despite the reduction in width, the NPL thickness remained nearly constant, between ∼4 and 7 nm, regardless of Mn content. Even at the smallest sizes, the NPLs preserved a well-defined hexagonal platelet morphology.

In addition to barium ferrite NPLs, the BFM-1.4 sample contained larger particles of secondary phases ranging from a few hundred nanometers to over 1 μm in size (Figure 3f). Two distinct morphologies of secondary phases were observed: hexagonal platelets (labeled "HP" in Figure 3f) and elongated rectangular crystals ("RC").

The composition of the phases was determined by quantifying the EDXS spectra collected from a large number of particles. The unsubstituted barium ferrite NPLs contained Ba and Fe in an atomic ratio of 7.3 ± 0.3:92.7 ± 0.3 (O not quantified). Analyses of the Mn-substituted NPLs confirmed the incorporation of Mn into the NPL structure. In the BFM-0.043 sample, the NPLs contained Ba, Fe, and Mn in an atomic ratio of 7.2 ± 0.3:89.4 ± 0.4:3.5 ± 0.3. This composition can be expressed, in terms of the chemical formula for bulk BHF, as $Ba_{0.94\pm0.04}Fe_{11.62\pm0.05}Mn_{0.46\pm0.04}O_{19}$. However, the NPLs exhibit a composition significantly different from that of the bulk, as will be further discussed in the Discussion section. The solid-solubility limit of Mn in barium ferrite NPLs was determined in the BFM-1.4 sample to correspond to a composition containing Ba, Fe, and Mn in an atomic ratio of 7.4 ± 0.3:67.9 ± 0.7:24.8 ± 0.5, corresponding to the bulk BHF formula $Ba_{0.96\pm0.04}Fe_{8.83\pm0.09}Mn_{3.22\pm0.07}O_{19}$.

The composition of the secondary phases in the BFM-1.4 sample varied considerably from particle to particle. For the hexagonal platelets, the Ba/Fe/Mn atomic ratio was 44.4 ± 2.7:9.1 ± 5.9:46.6 ± 3.7, consistent with the hexagonal perovskite formula $Ba_{0.89\pm0.05}Fe_{0.18\pm0.12}Mn_{0.89\pm0.08}O_x$. The rectangular crystals contained Ba, Fe, and Mn in the atomic ratio 23.9 ± 0.5:28.9 ± 6.2:47.2 ± 6.2, which corresponds reasonably well to Fe-substituted $BaMn_3O_6$, with the formula $Ba_{0.96\pm0.02}Fe_{1.16\pm0.25}Mn_{1.89\pm0.25}O_x$.

Upon annealing in ambient air, the NPLs underwent significant growth. After annealing for 2 h at 800 °C, the unsubstituted BHF NPLs ranged from approximately 100 nm to 1 μm in width and were several tens of nanometers thick (TEM images and XRD patterns of the annealed NPLs are shown in the SI). Mn substitution limited particle growth, resulting in smaller and more uniform NPLs. After annealing at 800 °C, the barium ferrite NPLs with lower Mn content (BFM-0.043) were approximately 100−250 nm wide (Figure S1b), whereas at higher Mn substitution (BFM-0.33) the NPLs were below 200 nm wide (Figure S1c). TEM/EDXS analysis of the annealed BFM-0.33 sample confirmed that the barium ferrite NPLs had a composition close to the nominal $BaFe_9Mn_3O_{19}$, but also revealed two secondary phases: (i) larger plate-like particles containing almost only Fe and O, and (ii) large rectangular particles with a Ba/Fe/Mn atomic ratio of approximately 24:43:32 (Figure S1d). XRD of this sample showed peaks corresponding to hematite and some unidentified phase(s), in addition to those of the hexaferrite NPLs (Figure S2). The origin of these secondary phases remains unclear.

After annealing for 2 h at 1000 °C, the NPLs in the unsubstituted sample grew to about 500 nm, while in the Mn-substituted samples their size remained around 300 nm. Larger

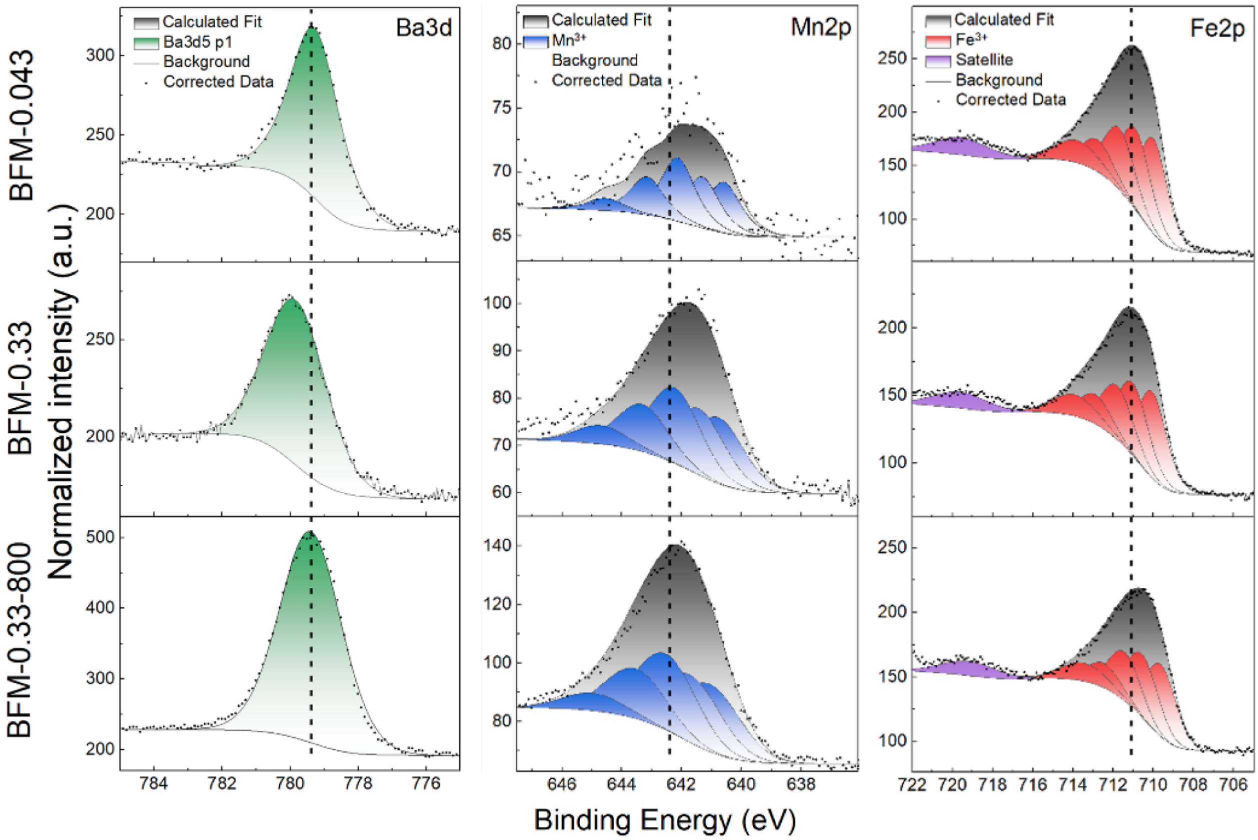

Figure 4. XPS spectra of BFM-0.043 and BFM-0.33 after hydrothermal synthesis and after subsequent annealing for 2 h at 800 °C (BFM-0.33-800).

secondary-phase particles were also present in the BFM-0.33 sample (Figure S3).

XPS analysis was used to determine the oxidation states of Mn and Fe in the Mn-substituted BHF NPLs. The hydrothermally synthesized NPLs with the lowest Mn concentration (BFM-0.043) and those with Mn content near the solid solubility limit (BFM-0.33) were compared with the BFM-0.33 NPLs annealed for 2 h at 800 °C, which resembled coarser particles (Figure 4).

The Ba $3d_{5/2}$ peak for BFM-0.043 NPLs was consistent with literature data,[54] with binding energy of 779.4 eV. This peak shifted upward by approximately 0.6 eV with increasing Mn content (BFM-0.33) and returned to 779.4 eV after annealing at 800 °C.

The Fe $2p_{3/2}$ region was fitted according to the procedure of Biesinger et al.,[55] using six components. The results confirmed that Fe was present in the 3+ oxidation state. For BFM-0.33, the peak positions were shifted slightly toward higher binding energies (~711 eV) relative to the reference data.[54] After annealing at 800 °C, the peak shifted to lower binding energies (~710.5 eV), consistent with reported values for $BaFe_{12}O_{19}$.[54] This shift indicates that the local environment of Fe^{3+} ions in the annealed sample closely resembles that in pure BHF.

The Mn region was fitted with five peaks, also according to Biesinger et al.[55] The best fit indicated Mn in the 3+ oxidation state, although partial reduction to Mn^{2+} could not be excluded. The fitting results suggested that up to ~30% of Mn may exist in the reduced state. Upon annealing, the Mn peaks shifted slightly toward higher binding energies (from 642.3 to 642.7 eV), indicating a modification in the local chemical environment of Mn ions. This shift can likely be ascribed, at least in part, to the formation of secondary phases observed by TEM, where Mn atoms form stronger bonds with oxygen.

The presence of Mn^{2+} was further supported by thermogravimetric analysis (TGA) of the Mn-substituted BFM-0.33 NPLs (Figure S4). Below ~600 °C, a total mass loss of approximately 4% was observed, attributed to the release of adsorbed and structurally bound water (<200 °C), carbonate species (<300 °C), and residual nitrate species (400−600 °C), consistent with previous reports.[56] Above 734 °C, a mass increase of 0.27% was detected, which is attributed to oxidation of Mn^{2+}. This mass gain corresponds to approximately 12.5% of the total Mn being present in the +2 oxidation state. The total mass gain may be underestimated due to partial overlap with a subsequent mass loss (see Supporting Information for details).

The Mn substitution had a profound influence on the magnetic properties of the NPLs. Figure 5a shows the room-temperature magnetic hysteresis loops of the NPLs after hydrothermal synthesis. The unsubstituted NPLs exhibited a relatively broad hysteresis loop, with a coercivity (H_C) of 63.7 kA/m and a moderate magnetization at a high field strength of 800 kA/m ($M_{800kA/m}$ = 19.3 Am^2/kg) (Figure 5a). With Mn substitution, the magnetic properties decreased drastically. Even at the lowest Mn content (BFM-0.043), $M_{800kA/m}$ dropped to 11.6 Am^2/kg and H_C decreased to 39.0 kA/m. At the composition near the Mn solid solubility limit in barium ferrite (BFM-0.33), the NPLs were weakly magnetic, with $M_{800kA/m}$ ~ 4 Am^2/kg and H_C = 2.3 kA/m.

Particle growth during annealing in ambient air improved the magnetic properties of the NPLs. After annealing at 800

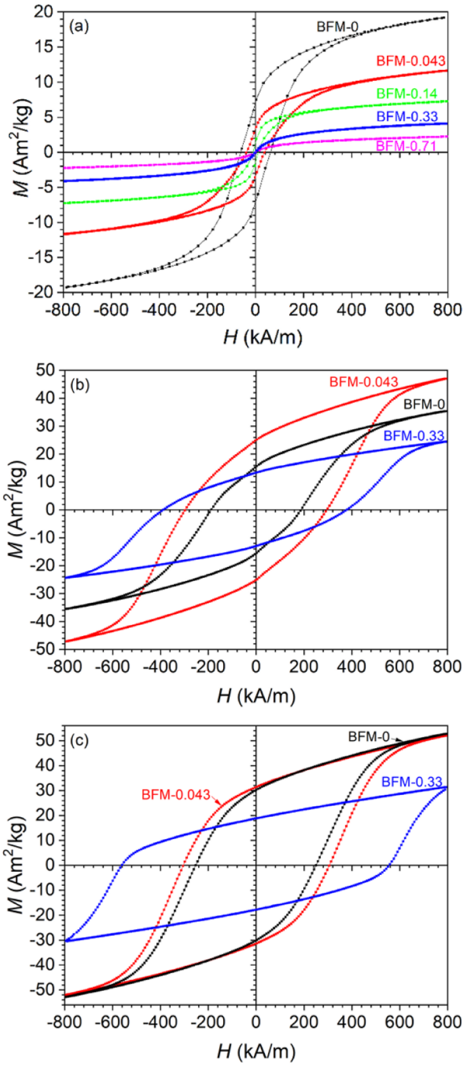

Figure 5. Room-temperature magnetic hysteresis loops for Mn-substituted BHF NPLs after the hydrothermal synthesis at 250 °C (a), and after subsequent annealing in an ambient air for 2 h at 800 °C (b) and 1000 °C (c).

°C, the unsubstituted NPLs (BFM-0) exhibited $M_{800\text{kA/m}}$ = 35.4 Am^2/kg and H_C = 63.7 kA/m (Figure 5b). Interestingly, the NPLs with lower Mn content (BFM-0.043) showed an even higher magnetization ($M_{800\text{kA/m}}$ = 47.1 Am^2/kg) compared to the unsubstituted sample, while those with higher Mn substitution (BFM-0.33) had much lower magnetization ($M_{800\text{kA/m}}$ = 24.4 Am^2/kg). Additionally, the coercivity of the Mn-substituted NPLs was significantly higher than that of the unsubstituted ones, reaching 298 kA/m for BFM-0.043 and 390 kA/m for BFM-0.33.

After annealing for 2 h at 1000 °C, the unsubstituted NPLs reached $M_{800\text{kA/m}}$ ~ 53 Am^2/kg and H_C ~ 250 kA/m (Figure 5c). The NPLs with lower Mn substitution showed a comparable $M_{800\text{kA/m}}$ but a somewhat higher H_C of ~ 305 kA/m. In contrast, the NPLs with higher Mn substitution exhibited a modest $M_{800\text{kA/m}}$ of 31.5 Am^2/kg but an exceptionally high H_C exceeding 560 kA/m. The increase in H_C with Mn substitution can be partially attributed to particle refinement. The observed decrease in M_S with Mn substitution in annealed barium ferrites is consistent with literature reports, as Mn is known to reduce the M_S of hexaferrite ceramics.[15,57,58]

To compare the magnetic properties of the NPLs with bulk materials, we prepared unsubstituted and highly Mn-substituted BHF ceramics (see SI for details). Substituting three Fe atoms with Mn ($BaFe_9Mn_3O_{19}$) reduced M_S by ~35% (Figure S5). In contrast, the decrease in M_S for the NPLs was much larger: at the same composition (Mn/Fe = 0.33), M_S dropped by more than 75% compared to the unsubstituted NPLs (Figure 5a). This pronounced reduction suggests a substantial change in the (magnetic) structure induced by Mn substitution in NPLs.

Structure of Mn-Substituted Barium Ferrite Nanoplatelets

The crystalline structure of barium ferrite NPLs was studied using atomic-resolution imaging with aberration-corrected STEM. After annealing at 800 °C, the magnetic properties of unsubstituted NPLs approached those of bulk BHF; therefore, a well-ordered crystal structure was expected for the annealed NPLs. Figure 6 shows STEM images of unsubstituted BHF NPLs after annealing for 2 h at 800 °C. The NPL is oriented along the <10$\bar{1}$0> direction of its hexagonal structure, with basal surfaces parallel to the electron beam. The experimental atomic-resolution HAADF image in Figure 6c is compared with the image calculated[59] based on the BHF structure. In HAADF images, the intensity of a spot representing an individual atomic column is roughly proportional to the square of the column's average atomic number Z (~Z$^\alpha$, with α slightly lower than 2).[59] Thus, columns containing the heavier Ba^{2+}

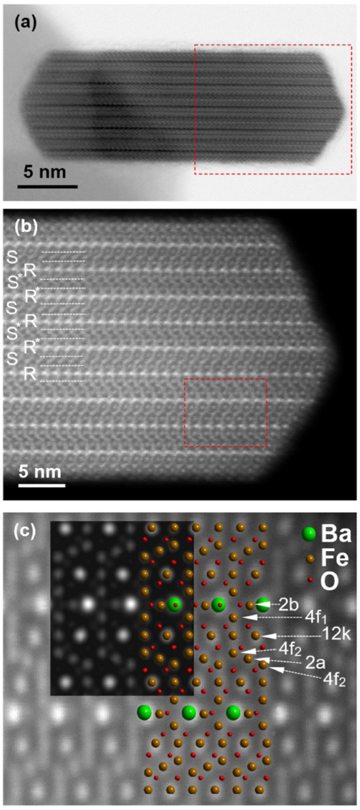

Figure 6. BF (a) and HAADF (b and c) STEM images of an unsubstituted barium ferrite NPL annealed for 2 h at 800 °C. Calculated image and a structural model of M-hexaferrite structure projected along [10$\bar{1}$0] direction is superimposed over the image (c) to illustrate the positions of the Ba, Fe and O atoms. The positions of five different Fe sites, i.e., tetrahedral (4f$_1$), octahedral (12k, 2a, 4f$_2$), and trigonal (2b) are marked.

ions can be clearly distinguished from those containing the lighter Fe^{3+} ions, while columns containing only O^{2-} ions are not visible. A projected model of the BHF structure is superimposed on the HAADF image in Figure 6c. All cationic lattice sites of the hexaferrite structure—i.e., Ba sites and the five different Fe sites—are clearly visible in the experimental HAADF images. The complete hexaferrite structure with all cationic positions is also clearly resolved in HAADF images of as-synthesized hexaferrite NPLs (Figure S6).

Remarkably, STEM imaging of the as-synthesized Mn-substituted barium ferrite NPLs revealed significant deviations from the regular M-hexaferrite structure. Figure 7a shows HAADF images of NPLs from the BFM-1.4 sample. A majority of the NPLs contained four Ba layers and were ~5 nm thick. Due to the smaller widths (~10−50 nm), the NPLs imaged in edge-on orientation made much thinner imaging objects than the wider, annealed unsubstituted NPLs. The thinner specimen resulted in improved resolution. All cationic columns of the hexaferrite structure were well resolved and clearly visible, except for the trigonal Fe(2b) columns (Figure 7b). At the positions corresponding to the Fe(2b) sites, no intensity above background was observed (the Fe(2b) positions are marked with cyan dots in the projected structural model superimposed on the experimental HAADF image in Figure 7b).

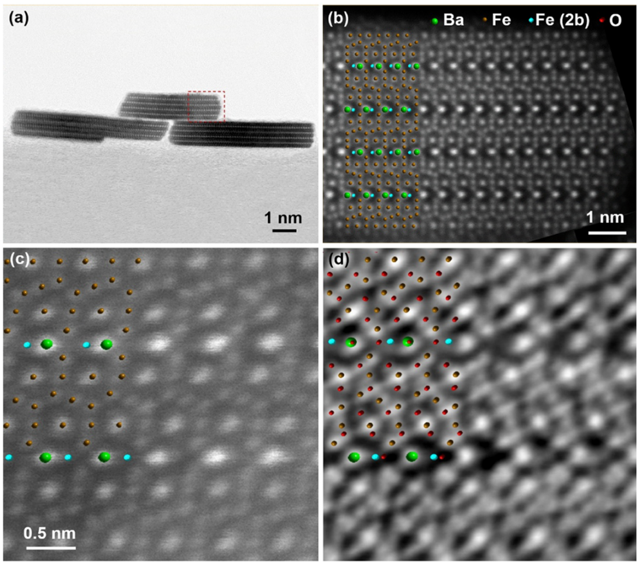

Figure 7. (a) BF and (b) HAADF STEM images of a Mn-substituted barium ferrite NPL from hydrothermally synthesized BFM-1.4 sample. The structural model of M-hexaferrite structure projected along $[10\bar{1}0]$ direction is superimposed over the image (b) to illustrate the positions of the Ba and Fe atoms. (c) HAADF and (d) iDPC STEM images of a NPL from the BFM-0.33 sample. The positions of the Ba, Fe and O columns on the images (c, d) are marked with red, brown/cyan and red dots, respectively.

Figure 7c, d shows simultaneously recorded HAADF and iDPC images of a barium ferrite NPL from the BFM-0.33 sample. The iDPC technique enables direct imaging of the phase of the transmission function, which can be directly interpreted as the projected electrostatic potential. The contrast in iDPC images is approximately linearly proportional to the atomic number Z, allowing simultaneous visualization of both heavy and light atoms in the same image of a thin sample.[60] The arrangement of dots in the iDPC image in Figure 7d corresponds well to the hexaferrite structure, with the notable exception of the Fe(2b) positions. The Fe(2b) columns are absent in a large proportion of the inspected NPLs' area. Moreover, in addition to the Fe(2b) columns, the neighboring O columns are also missing. Only in certain regions of the NPL was a very weak, diffuse contrast observed at the approximate positions of the Fe(2b) and adjacent O columns.

After annealing for 2 h at 800 °C, the structure of the Mn-substituted NPLs was restored. In the HAADF image of a NPL from the annealed BFM-0.33 sample (Figure 8), all cationic columns are clearly visible, including the Fe(2b) sites.

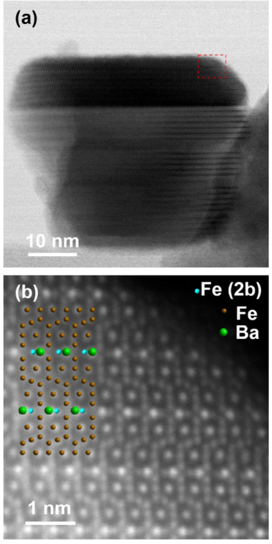

Figure 8. BF (a) and HAADF (b) STEM images of a NPL from the BFM-0.33 sample annealed for 2 h at 800 °C.

It is expected that the (partially) unoccupied Fe(2b) lattice sites observed in the substituted NPLs are accompanied by other structural distortions. Measurements of the periodicity across the NPL structure on HAADF images of the as-synthesized and annealed BFM-0.33 samples revealed significant differences. The R blocks were significantly wider in the as-synthesized NPLs than in the annealed NPLs, while the width of the S block remained similar. (The block width was measured as the distance between two consecutive Fe(12k) rows, considering only blocks located in the interior of the NPLs.)

Measurements from several images showed R- and S-block widths of 6.8 ± 0.4 Å and 5.0 ± 0.3 Å, respectively, for the as-synthesized NPLs, and 6.3 ± 0.3 Å and 5.0 ± 0.3 Å for the annealed NPLs. For comparison, in unsubstituted bulk BHF, the R and S blocks are theoretically 6.7 Å and 5.1 Å wide, respectively. The observed differences in lattice spacing can be attributed to vacant atom positions, which induce local lattice expansion in order to minimize electrostatic repulsions in their vicinity.[61,62]

Elemental EDXS mapping (Figure 9) indicated an even distribution of Mn across all Fe lattice sites in the as-synthesized NPLs. The Ba signal clearly coincided with the Ba-containing rows, while the Fe (and Mn) signals decreased at these rows, consistent with the absence of 2b sites in the structure of the as-synthesized, Mn-substituted NPLs. The revealed distribution of Fe and Mn suggests that Mn

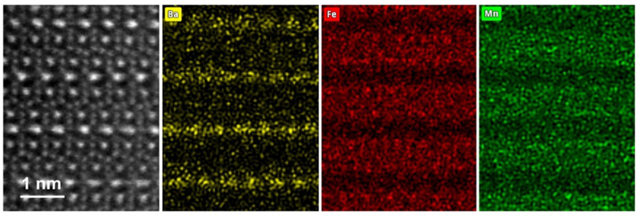

Figure 9. HAADF STEM image of a NPL's hexaferrite structure with corresponding EDXS elemental maps showing the distribution of Ba, Fe and Mn. The BFM-1.4 sample was hydrothermally synthesized, without annealing.

substitutes into all available Fe sites. Previous studies reported that, in bulk hexaferrite, Mn occupies all Fe sites except the trigonal 2b sites, which are unoccupied in the NPLs.[17−19]

Deviations from the ideal M-hexaferrite structure were observed even at the lowest Mn substitution. The BFM-0.043 sample consisted of smaller primary NPLs and larger NPLs formed by Ostwald ripening (Figure 3b). The smaller NPLs exhibited the SRS* structure characteristic of primary barium hexaferrite NPLs,[4] whereas most of the larger NPLs contained only two Ba layers (i.e., an SRS*R*S structure across NPL's thickness) and, less frequently, three Ba layers. These NPLs were therefore thinner but considerably wider than the heavily Mn-substituted ones. The greater lateral dimensions of these NPLs increased the local sample thickness, which reduced the achievable resolution. Nevertheless, the analysis indicates that the Fe(2b) sites were not fully occupied (Figure S7).

The NPL structure was further characterized by Raman spectroscopy. Figure 10 shows the Raman spectra of unsubstituted NPLs (BFM-0) and highly Mn-substituted (BFM-0.33) after hydrothermal synthesis and after subsequent annealing for 2 h at 800 °C (positions of the Raman peaks are listed in the SI, Table S1). The unsubstituted NPLs exhibit only seven clear Raman modes, which correspond well to the sintered reference, though with some softening and broadening. The broadening can be attributed to a higher degree of structural disorder, while the softening is most likely extrinsic, caused by Raman-laser heating. In the as-synthesized BFM-0 the missing modes around 200 cm^{-1} correspond to vibrations of the entire spinel block, and the missing mode around 467 cm^{-1} corresponds to FeO_6 octahedral vibrations.[63] These modes reappear after annealing, and the line widths become narrower, indicating reduced structural disorder.

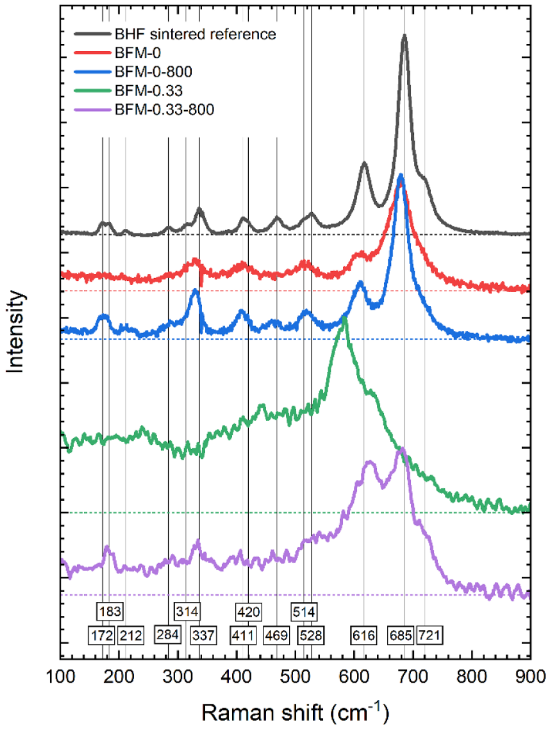

Figure 10. Room-temperature Raman spectra for unsubstituted barium ferrite NPLs (BFM-0) and Mn-substituted BHF NPLs (BFM-0.33) after hydrothermal synthesis, and after annealing for 2 h at 800 °C in an ambient air. The spectra are vertically scaled for easier comparison.

The as-synthesized Mn-substituted NPLs display a completely distorted spectrum: a broad continuum extending up to ~800 cm^{-1} with a broad peak at 580 cm^{-1}. This indicates the absence of long-range order, as finite-momentum modes become optically active. Notably, the spectral weight around 680 cm^{-1}, associated with the $Fe(2b)O_5$ bipyramidal Ag mode,[63] is missing. This absence correlates with the lack of Fe(2b) columns observed in the STEM images. Annealing partially suppresses the broad continuum and restores the $Fe(2b)O_5$ bipyramids, resulting in the recovery of the 680 cm^{-1} mode, consistent with the reappearance of Fe(2b) columns in the STEM images.

Other expected BHF modes also become discernible from the continuum after annealing, particularly the second strongest BHF mode at 618 cm^{-1}, as well as the 721, 528, and 337 cm^{-1} modes. The modes around 200 cm^{-1}, corresponding to vibrations of the entire spinel block, also become clear and as narrow as in the reference ceramic pellet. The partial suppression of the continuum indicates improved long-range structural coherence, although the high-frequency oxygen modes remain broader than in the unsubstituted NPLs. This broadening can likely be attributed to local site disorder introduced by Mn−Fe substitution.

First-Principles Modeling Results

In order to gain further insight into the structure, we performed DFT calculations of Mn substitution in bulk BHF. As a first step, we substituted one Fe^{3+} ion with a Mn ion at each of the five different sites in the BHF unit cell (shown in Figure 11a). We find that substitution is most favorable at the 12k and 2a sites, with a ΔE_{subs} of −2.9 eV. In contrast, a single Mn substitution at the $4f_2$ and $4f_1$ sites is less favorable, with ΔE_{subs} values of −2.7 eV and −2.6 eV, respectively. The least favorable site is 2b, with ΔE_{subs} = −2.5 eV. These results are consistent with previously reported experimental observations.[17−19]

Next, we considered the vacancy formation energy for a single Fe atom at the respective sites in pristine and Mn-substituted BHF bulk. In pristine BHF, we obtained the highest vacancy formation energies at the 2b and 12k sites, with values of 1.6 eV, while slightly lower values of about 1.3 eV were found for the $4f_1$, $4f_2$, and 2a sites. Vacancy formation becomes even less favorable in Mn-substituted BHF, where we obtained the highest value of 3.9 eV for the $4f_2$ site, followed by 3.4 eV for the 2b site and 3.3 eV for the $4f_1$ site, while at the 12k and 2a sites ΔE_{vac} is about 3.0 eV. These results indicate that the formation of a 2b vacancy is particularly unfavorable.

Given that iDPC imaging results showed the depletion of Fe(2b) in the structure of barium ferrite NPLs is accompanied

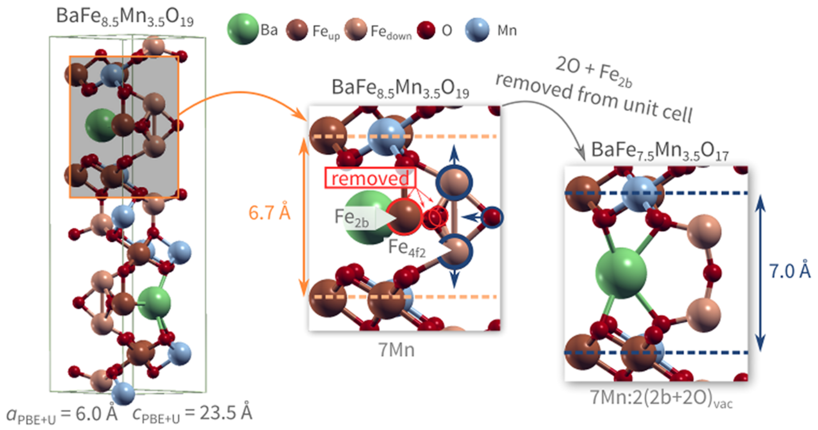

Figure 11. Bulk unit cell of the Mn substituted M-type barium hexaferrite, with the optimized lattice parameters obtained using DFT+U indicated below. The created vacancies and associated ionic displacements (marked with red arrows) leading to formation of the $7Mn{:}2(2b+2O)_{vac}$ from the 7Mn structure are highlighted in the middle close-up. The relaxed atomic structure in the vicinity of the defect complex is shown in the right-hand close-up. Note that the interlayer distance between the Fe(12k) sites increases by 0.3 Å for the $7Mn{:}2(2b+2O)_{vac}$ structure.

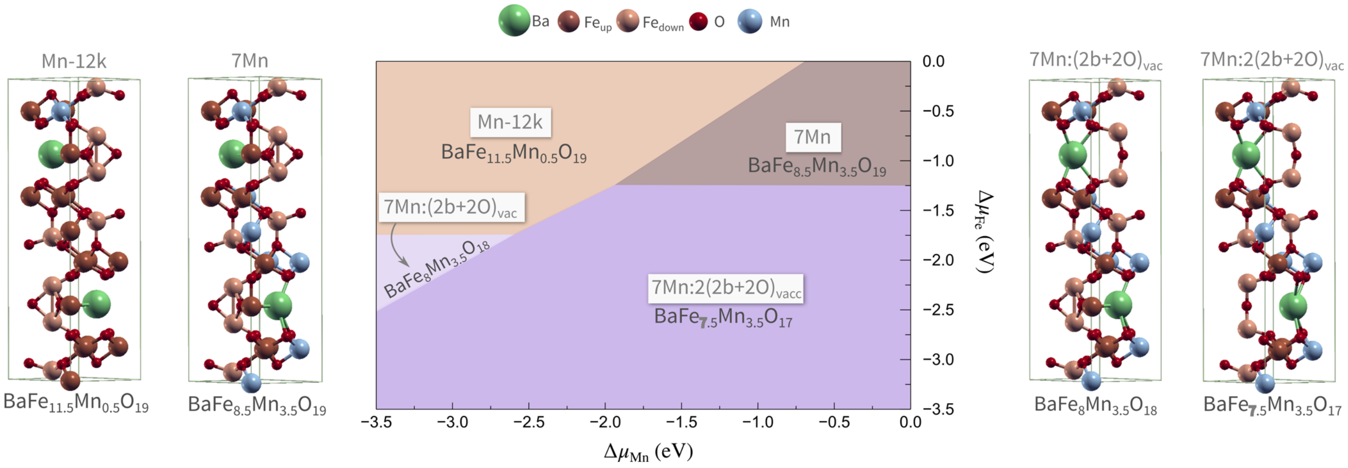

Figure 12. Phase diagram of different Mn-substituted and vacancy-containing structures of bulk BHF, as a function of the Fe ($\Delta\mu_{Fe}$) and Mn ($\Delta\mu_{Mn}$) chemical potentials. The unit cells of the phases appearing in the phase diagram, together with their corresponding labels, are shown on the left- and right-hand sides of the plot. The regions of different color indicate the most stable phase for a given combination of chemical potentials. At high Fe and Mn chemical potentials, the bulk-substituted 7Mn phase is the most stable, whereas at lower Fe chemical potentials (Fe-poor conditions), the 2b vacancy-containing phase becomes dominant.

by the formation of oxygen vacancies, we further considered the removal of an Fe atom at the 2b site along with its two nearest-neighbor oxygen atoms, designated as $Mn{:}(2b+2O)_{vac}$. We find that the formation of this defect complex is more favorable than the removal of a single Fe ion, with a ΔE_{vac} value of 2.2 eV. To examine whether a higher degree of Mn substitution affects this value, we substituted seven Fe ions in the bulk unit cell with Mn at the 12k and 2a sites, corresponding to a bulk stoichiometry of $BaFe_{8.5}Mn_{3.5}O_{19}$, which we designate as 7Mn (note that the bulk BHF unit cell contains two formula units). For this structure, the $(2b+2O)_{vac}$ formation energy is even lower, with a value of 1.9 eV. Finally, since there are two 2b sites in the bulk unit cell, we also considered the formation of two such defect complexes. For this structure, designated as $7Mn{:}2(2b+2O)_{vac}$, we obtain a ΔE_{vac} value of 3.4 eV (equivalent to 1.7 eV per defect complex). The construction of this defect configuration is summarized on the right-hand side of Figure 11, while the fully relaxed atomic structure is shown in Figure 12. The formation of one such defect complex leads to an increase in the 12k interlayer distance from 6.7 Å to 7.0 Å, which is consistent with the structural deformations observed in HAADF images of the as-synthesized Mn-substituted NPLs described in the previous section.

The results of the atomistic thermodynamics analysis, as defined in eq 4, are shown in Figure 12, where the thermodynamically most stable phase is plotted for a given combination of Fe ($\Delta\mu_{Fe}$) and Mn ($\Delta\mu_{Mn}$) chemical potentials (the unit cells of the considered defected structure are presented on the left- and right-hand sides of the phase diagram). We find that, under Fe-rich and Mn-rich conditions (i.e., when both chemical potentials are high), the most stable phase is 7Mn, which has the same structure as bulk BHF, with a stoichiometry of $BaFe_{8.5}Mn_{3.5}O_{19}$. However, at low values of the iron chemical potential, the $7Mn{:}2(2b+2O)_{vac}$, with the stoichiometry of $BaFe_{7.5}Mn_{3.5}O_{17}$, becomes thermodynamically preferred. These results therefore indicate that this phase can be stabilized under specific conditions, particularly at higher Mn/Fe ratios.

■ DISCUSSION

Atomic-resolution STEM imaging and Raman spectroscopy revealed that the Fe(2b) lattice sites remain unoccupied in hydrothermally synthesized, highly Mn-substituted barium ferrite NPLs. First-principles modeling further indicated that vacancy complexes consisting of the missing Fe(2b) atom and two neighboring oxygen atoms ($(2b+2O)_{vac}$) are likely to form at higher Mn/Fe ratios. A derivative of the M-type hexaferrite structure in which the 2b sites remain unoccupied is known as the β-alumina structure (ideally $Me^+Al_{11}O_{17}$, where Me^+ represents alkali ion, Ag^+).[64] In β-alumina, spinel blocks alternate with Me^+ layers. Substitution of Al^{3+} with Fe^{3+} yields β-ferrites ($Me^+Fe_{11}O_{17}$; $P6_3/mmc$, $a = 0.557$ nm, $c = 2.26$ nm; see Figure 1b).[12−14] These β-ferrites are antiferromagnetic (with $T_N \sim 713$ K for $KFe_{11}O_{17}$) because the two ferrimagnetic spinel blocks in the unit cell exhibit opposite magnetic moments.[65] At the small thicknesses characteristic of NPLs, however, this antiferromagnetic coupling is expected to be incomplete—particularly for an odd number of S blocks across the NPL—resulting in weak ferrimagnetism.

The $7Mn{:}2(2b+2O)_{vac}$ defected structure (Figure 11b) obtained as the result of first-principles modeling for the $BaFe_{8.5}Mn_{3.5}O_{19}$ composition closely resembles the β-ferrite structure. Moreover, HAADF images calculated[58] based on the $7Mn{:}2(2b+2O)_{vac}$ modeled structure matched very well with the experimental images, as shown on Figure 13.

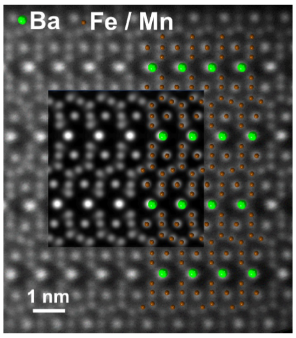

Figure 13. HAADF STEM image calculated based on the $7Mn{:}2(2b+2O)_{vac}$ modeled structure is compared with experimental image of a NPL from hydrothermally synthesized BFM-1.4 sample. A model of the structure projected along $[10\bar{1}0]$ direction is superimposed over the images (to illustrate the positions of the Ba, Fe/Mn atoms.

To the best of our knowledge, the Mn-substituted Ba^{2+} β-ferrite NPLs represent the first report of a pure Ba^{2+} β-ferrite analogue. Even though the NPLs were synthesized in concentrated NaOH, EDXS analysis showed no incorporation of Na into their structure. There have been reports of β-ferrites containing mixed Ba and alkali ions; however, these materials actually represent intergrowths of Ba-rich M-type hexaferrite domains and alkali-ion-rich β-ferrite domains.[67,68] In the case of the Mn-substituted Ba^{2+} β-ferrite NPLs, the extra positive charge introduced by replacing alkali ions with Ba^{2+} can be compensated by the partial reduction of Mn^{3+} according to $Ba^{2+}Fe^{3+}{}_{10-x}Mn^{3+}{}_xMn^{2+}O_{17}$. XPS analysis suggested that Mn is predominantly in the 3+ oxidation state; however, a small deviation from this value cannot be excluded. Alternatively, charge balance within the Ba^{2+} β-ferrite structure may be maintained by a nonstoichiometric composition, as β-ferrites are known to tolerate substantial deviations from the ideal $Me^+Fe_{11}O_{17}$ stoichiometry.[12−14,65,66]

Stabilization of the Ba^{2+} β-ferrite structure via proton incorporation at vacant Fe(2b) sites is also conceivable. However, FTIR analysis provides no evidence for lattice-incorporated hydroxyl species. The IR absorbance above 400 cm^{-1} in the NPLs is dominated with the three characteristic barium hexaferrite E_{1u} bands at 417, 443, and 568 cm^{-1}.[69] The observed O−H stretching bands are attributable to adsorbed surface water (see the SI for details).

The composition of the NPLs was determined by quantitative EDXS analysis. Interpretation of these results, however, is not straightforward because the composition of hexaferrite NPLs depends on their thickness. In general, the NPLs are Fe-rich relative to bulk $BaFe_{12}O_{19}$ hexaferrite because they always terminate on basal surfaces with Fe-only S structural blocks. The theoretical composition of the thinnest SRS*-structured M-hexaferrite NPLs (see the smaller NPL in Figure S7) can be described by the chemical formula $BaFe_{18}O_{28}$, whereas NPLs with an SRS*R*S structure (the larger NPL in Figure S7) exhibit a theoretical composition of $BaFe_{15}O_{23.5}$. With increasing thickness, the composition of the NPLs approaches that of bulk $BaFe_{12}O_{19}$.[4,9] Analogously, the composition of β-ferrite NPLs is Fe-rich compared with the ideal $BaFe_{11-x}Mn_xO_{17}$ bulk.

The highly Mn-substituted NPLs (samples BFM ≥ 0.33) typically contained four Ba layers. Their theoretical composition can be therefore expressed either using the M-hexaferrite formula $BaFe_{13.5-x}Mn_xO_{21.25}$ or the β-ferrite formula $BaFe_{12.5-x}Mn_xO_{19.25}$. The composition of the NPLs in the BFM-1.4 sample, obtained from EDXS analysis (Ba:Fe:Mn = 7.4 ± 0.3:67.9 ± 0.7:24.8 ± 0.5), closely matches the β-ferrite formula $Ba_{1.00\pm0.04}Fe_{9.17\pm0.10}Mn_{3.35\pm0.07}O_x$ (assuming NPLs contain four Ba layers). The measured (Fe + Mn)/Ba ratio of 12.53 ± 0.68 agrees well with the theoretical ratio for the β-ferrite NPLs ((Fe + Mn)/Ba = 12.5), but is lower than that expected for M-type hexaferrite NPLs ((Fe + Mn)/Ba = 13.5).

At low Mn substitution levels, the NPLs were thinner. Assuming NPLs containing only two Ba layers, which were frequently observed in the BFM-0.043 sample, their theoretical composition can be described either by the M-type hexaferrite formula $BaFe_{15-x}Mn_xO_{23.5}$ or as the β-ferrite formula $BaFe_{14-x}Mn_xO_{22}$. The (Fe + Mn)/Ba ratio measured with EDXS for the BFM-0.043 sample (12.90 ± 0.64) is closer to the β-ferrite theoretical value ((Fe + Mn)/Ba = 14) than to that of M-hexaferrite ((Fe + Mn)/Ba = 15), although the exact average thickness of the NPLs remains uncertain.

The experimental results cannot exclude incomplete depletion of the Fe(2b) lattice sites, particularly at lower levels of Mn substitution. In this case, the structure of the NPLs can be regarded as a defected M-type hexaferrite structure $(Ba^{2+}Fe^{3+}{}_{12-x-y}Mn^{3+}{}_x(\square_{Fe(2b)})_yO_{19-1.5y}(\square_O)_{1.5y}$, where $\square$ represent a vacancy).

A Fe(2b)-vacant M-type structure has previously been observed after irradiation of BHF single crystals and ceramics with fast neutrons.[70] The 2b sites are critical for the high magnetocrystalline anisotropy of M-type hexaferrites.[7] Vacancies at these sites disrupt the collinear magnetic ordering by weakening the exchange interactions between the spinel blocks and, as a result, markedly reduce the magnetization.[7,70]

Upon annealing at 800 °C, the M-type hexaferrite structure was restored. STEM imaging and Raman spectroscopy clearly revealed signals associated with the Fe(2b) lattice sites, along with magnetic properties characteristic of Mn-substituted M-type hexaferrite. The restoration of the M-type structure is likely related to changes in the composition, which is most probably maintained by precipitation of excess Ba as a Ba-rich secondary phase. After annealing of the BFM-0.33 sample, XRD and TEM analyses confirmed the presence of secondary phases; however, their origin remains unclear and may not be related solely to the β-ferrite → M-hexaferrite transformation. With the thickening of NPLs upon annealing, excess Fe^{3+} precipitates because the composition changes from Fe-rich NPLs to stoichiometric bulk.[71]

CONCLUSIONS

Mn-substituted barium ferrite nanoplatelets (NPLs) were synthesized by hydrothermal treatment of an aqueous suspension of the corresponding hydroxides at 250 °C. EDXS analysis revealed that up to ~27% of Fe can be substituted by Mn in the NPL structure. Increasing Mn substitution resulted in a decrease in nanoplatelet size and a more uniform size distribution. Highly Mn-substituted NPLs were approximately 10−50 nm wide and 4−6 nm thick as opposed to the unsubstituted NPLs, which were ~100−800 nm wide and ~10 nm thick.

The magnetic properties of the NPLs—coercivity and high-field magnetization—decreased markedly with Mn substitution. Structural analysis using aberration-corrected STEM in combination with Raman spectroscopy showed that the unsubstituted NPLs exhibited the regular M-type hexaferrite structure, whereas Mn substitution induced notable structural changes. In particular, HAADF imaging revealed that the Fe(2b) trigonal lattice sites of the M-type hexaferrite structure were unoccupied in the Mn-substituted NPLs. Furthermore, iDPC imaging indicated that depletion of Fe(2b) sites in the NPL structure was accompanied by the formation of neighboring oxygen vacancies.

The experimental observations were supported with first-principles modeling, which demonstrated that the formation energy of vacancy complexes comprising unoccupied Fe(2b) sites and two adjacent oxygen sites decreases with increasing Mn substitution, leading to the thermodynamic stabilization of this defected structure at higher Mn/Fe ratios. The defected structure predicted by modeling shares structural features with a β-alumina-type ferrite structure, which typically forms with alkali ions Me^+ ($Me^+Fe_{11}O_{17}$). To the best of our knowledge, the Mn-substituted barium ferrite NPLs reported here represent the first observation of a pure Ba^{2+} β-ferrite analogue.

Upon annealing at 800 °C, the M-type hexaferrite structure was restored, and the Mn-substituted NPLs recovered the magnetic properties characteristic of M-type Mn-substituted barium hexaferrite.

ASSOCIATED CONTENT

Supporting Information

The Supporting Information is available free of charge at https://pubs.acs.org/doi/10.1021/acs.chemmater.6c00103.

> Additional information on characterization and used materials, TEM and XRD characterization of annealed materials, thermal analysis, magnetic properties of ceramic references, HAADF STEM images of unsubstituted barium ferrite nanoplatelets and nanoplatelets at the lowest Mn substitution, details of Raman analysis, and FTIR analysis (PDF)

AUTHOR INFORMATION

Corresponding Author

Darko Makovec − *Jožef Stefan Institute, Ljubljana SI-1000, Slovenia;* orcid.org/0000-0002-0190-6758;
Email: darko.makovec@ijs.si

Authors

Matic Poberžnik − *Jožef Stefan Institute, Ljubljana SI-1000, Slovenia;* orcid.org/0000-0002-4866-4346
Janvit Teržan − *National Institute of Chemistry, Ljubljana SI-1000, Slovenia;* orcid.org/0000-0001-5528-5355
Tomaž Mertelj − *Jožef Stefan Institute, Ljubljana SI-1000, Slovenia; Center of Excellence on Nanoscience and Nanotechnology Nanocenter (CENN Nanocenter), Ljubljana 1000, Slovenia*
Damjan Vengust − *Jožef Stefan Institute, Ljubljana SI-1000, Slovenia*
Goran Dražić − *National Institute of Chemistry, Ljubljana SI-1000, Slovenia;* orcid.org/0000-0001-7809-8050
Darja Lisjak − *Jožef Stefan Institute, Ljubljana SI-1000, Slovenia;* orcid.org/0000-0003-4154-4592
Sašo Gyergyek − *Jožef Stefan Institute, Ljubljana SI-1000, Slovenia;* orcid.org/0000-0002-7325-2984

Complete contact information is available at: https://pubs.acs.org/10.1021/acs.chemmater.6c00103

Author Contributions

The manuscript was written through contributions of all authors. All authors have given approval to the final version of the manuscript.

Notes

The authors declare no competing financial interest.

ACKNOWLEDGMENTS

The authors acknowledge the financial support from the Slovenian Research Agency (research core funding no. P2-0089).

REFERENCES

(1) Makovec, D. Adaptation of the Crystal Structure to the Confined Size of Mixed-Oxide Nanoparticles. *Acta Chim. Slov.* **2022**, *69*, 756−771.

(2) Navrotsky, A. Energetic Clues to Pathways to Biomineralization: Precursors, Clusters, and Nanoparticles. *Proc. Natl. Acad. Sci. U. S. A.* **2004**, *101*, 12096−12101.

(3) Makovec, D.; Križaj, N.; Meden, A.; Dražić, G.; Uršič, H.; Kostanjšek, R.; Šala, M.; Gyergyek, S. Ferroelectric Bismuth-Titanate Nanoplatelets and Nanowires with a New Crystal Structure. *Nanoscale* **2022**, *14*, 3537−3544.

(4) Makovec, D.; Belec, B.; Goršak, T.; Lisjak, D.; Komelj, M.; Dražić, G.; Gyergyek, S. Discrete Evolution of the Crystal Structure during the Growth of Ba-Hexaferrite Nanoplatelets. *Nanoscale* **2018**, *10*, 14480−14491.

(5) Makovec, D.; Dražić, G.; Gyergyek, S.; Lisjak, D. A New Polymorph of Strontium Hexaferrite Stabilized at the Nanoscale. *CrystEngComm* **2020**, *22*, 7113−7122.

(6) Smith, J.; Wijn, H. P. J. *Ferrites: Physical Properties of Ferromagnetic Oxides in Relation to Their Technical Applications*; Philips'Technical Library: Eindhoven, 1959.

(7) Pullar, R. C. Hexagonal Ferrites: A Review of the Synthesis, Properties and Applications of Hexaferrite Ceramics. *Prog. Mater. Sci.* **2012**, *57*, 1191−1334.

(8) Poberžnik, M.; Herrero-Saboya, G.; Makovec, D.; Lisjak, D.; Martin-Samos, L. Surface Phase Diagrams of Pristine and Hydroxylated Barium Hexaferrite Surfaces from First-Principles Atomistic Thermodynamics. *Appl. Surf. Sci.* **2023**, *637*, 157890.

(9) Belec, B.; Dražić, G.; Gyergyek, S.; Podmiljšak, B.; Goršak, T.; Komelj, M.; Nogués, J.; Makovec, D. Novel Ba-Hexaferrite Structural Variations Stabilized on the Nanoscale as Building Blocks for Epitaxial Bi-Magnetic Hard/Soft Sandwiched Maghemite/Hexaferrite/Maghemite Nanoplatelets with Out-of-Plane Easy Axis and Enhanced Magnetization. *Nanoscale* **2017**, *9*, 17551−17560.

(10) Makovec, D.; Komelj, M.; Dražić, G.; Belec, B.; Goršak, T.; Gyergyek, S.; Lisjak, D. Incorporation of Sc into the Structure of Barium-Hexaferrite Nanoplatelets and Its Extraordinary Finite-Size Effect on the Magnetic Properties. *Acta Mater.* **2019**, *172*, 84−91.

(11) Lisjak, D.; Drofenik, M. Chemical Substitution—An Alternative Strategy for Controlling the Particle Size of Barium Ferrite. *Cryst. Growth Des.* **2012**, *12*, 5174−5179.

(12) Boilot, J. P.; Colomban, P.; Collin, G.; Comes, R. Crystal structure and ion-ion correlation in ion-rich β alumina type compounds. II. potassium β ferrite II. Potassium β-Ferrite. *Solid State Ionics* **1980**, *1* (1−2), 69−76.

(13) Ito, S.; Kubo, N.; Nariki, S.; Yoneda, N. Ion Exchange in Alkali Layers of Potassium β-Ferrite ($(1 + x)K_2O\cdot 11Fe_2O_3$) Single Crystals. *J. Am. Ceram. Soc.* **1987**, *70*, 874−879.

(14) Ito, S.; Ui, K.; Koura, N.; Akashi, K. Lithium Secondary Battery Using Potassium-β-Ferrite as a New Cathode Active Material. *Solid State Ionics* **1998**, *113−115*, 17−21.

(15) Obradors, X.; Collomb, A.; Pernet, M.; Joubert, J. C.; Isalgue, A. Structural and Magnetic Properties of $BaFe_{12-x}Mn_xO_{19}$ Hexagonal Ferrite. *J. Magn. Magn. Mater.* **1984**, *44*, 118−128.

(16) Jirák, Z.; Pollert, E.; Vratislav, S. The Cooperative Jahn−Teller Effect in $BaFe_{2.5}Mn_{9.5}O_{19}$. *Phys. B* **1993**, *183*, 96−102.

(17) Collomb, A.; Obradors, X.; Isalgue, A.; Fruchart, D. Neutron Diffraction Study of the Crystallographic and Magnetic Structures of the $BaFe_{12-x}Mn_xO_{19}$ M-Type Hexagonal Ferrites. *J. Magn. Magn. Mater.* **1987**, *69*, 317−324.

(18) Jirák, Z.; Krupka, M.; Pollert, E. Cation Distribution in Hexaferrites $BaFe_{12-x}Mn_xO_{19}$. *Cryst. Res. Technol.* **1987**, *22*, K71−K73.

(19) Nemrava, S.; Vinnik, D. A.; Hu, Z.; Valldor, M.; Kuo, C.-Y.; Zherebtsov, D. A.; Gudkova, S. A.; Chen, C.-T.; Tjeng, L. H.; Niewa, R. Three Oxidation States of Manganese in the Barium Hexaferrite $BaFe_{12-x}Mn_xO_{19}$. *Inorg. Chem.* **2017**, *56*, 3861−3866.

(20) Zhai, K.; Wu, Y.; Shen, S.; Tian, W.; Cao, H.; Chai, Y.; Chakoumakos, B. C.; Shang, D.; Yan, L.; Wang, F.; et al. Giant Magnetoelectric Effects Achieved by Tuning Spin Cone Symmetry in Y-Type Hexaferrites. *Nat. Commun.* **2017**, *8*, 519.

(21) Lisjak, D.; Mertelj, A. Anisotropic Magnetic Nanoparticles: A Review of Their Properties, Syntheses and Potential Applications. *Prog. Mater. Sci.* **2018**, *95*, 286−328.

(22) Mertelj, A.; Lisjak, D.; Drofenik, M.; Čopič, M. Ferromagnetism in Suspensions of Magnetic Platelets in Liquid Crystal. *Nature* **2013**, *504*, 237−241.

(23) Mertelj, A.; Lisjak, D.; Osterman, N.; Čopič, M. Magneto-Optic and Converse Magnetoelectric Effects in a Ferromagnetic Liquid Crystal. *Soft Matter* **2014**, *10*, 9065−9072.

(24) Sahoo, R.; Rasna, M. V.; Lisjak, D.; Mertelj, A.; Dhara, S. Magnetodielectric and Magnetoviscosity Response of a Ferromagnetic Liquid Crystal at Low Magnetic Fields. *Appl. Phys. Lett.* **2015**, *106*, 161905.

(25) Shuai, M.; Klittnick, A.; Shen, Y.; Smith, G. P.; Tuchband, M. R.; Zhu, C.; Petschek, R. G.; Mertelj, A.; Lisjak, D.; Čopič, M.; et al. Spontaneous Liquid Crystal and Ferromagnetic Ordering of Colloidal Magnetic Nanoplates. *Nat. Commun.* **2016**, *7*, 10394.

(26) Tručl, J.; Hribar Boštjančič, P.; Gregorin, Ž.; Medle Rupnik, P.; Mertelj, A.; Lisjak, D. Ferromagnetic Ferrofluids in Aqueous and Low-Polar Media. *J. Colloid Interface Sci.* **2026**, *702*, 138806.

(27) Nádasi, H.; Medle Rupnik, P.; Küster, M.; Jarosik, A.; Tuffin, R.; Bremer, M.; Klasen-Memmer, M.; Lisjak, D.; Sebastián, N.; Mertelj, A.; et al. Room-Temperature Multiferroic Liquids: Ferroelectric and Ferromagnetic Order in a Hybrid Nanoparticle−Liquid Crystal System. *Adv. Mater.* **2025**, *37*, No. e08406.

(28) Kushnir, S. E.; Gavrilov, A. I.; Kazin, P. E.; Grigorieva, A. V.; Tretyakova, Y. D.; Jansen, M. Synthesis of Colloidal Solutions of $SrFe_{12}O_{19}$ Plate-Like Nanoparticles Featuring Extraordinary Magnetic-Field-Dependent Optical Transmission. *J. Mater. Chem.* **2012**, *22*, 18893−18901.

(29) Eliseev, A. A.; Eliseev, A. A.; Trusov, L. A.; Chumakov, A. P.; Boesecke, P.; Anokhin, E. O.; Vasiliev, A. V.; Sleptsova, A. E.; Gorbachev, E. A.; Korolev, V. V.; et al. Rotational Dynamics of Colloidal Hexaferrite Nanoplates. *Appl. Phys. Lett.* **2018**, *113*, 131106.

(30) Budinski, V.; Pevec, S.; Čampelj, S.; Mertelj, A.; Lisjak, D.; Đonlagić, D. Miniature Magneto-Optic Angular Position Sensor. *Opt. Lett.* **2022**, *47*, 4696−4699.

(31) Gregorin, T.; Budinski, V.; Pevec, S.; Njegovec, M.; Lisjak, D.; Mertelj, A.; Đonlagić, D. Miniature All-Fiber Electric Current/Magnetic Field Sensor Based on Birefringence Induced in Magneto-Optic Liquid. *IEEE Trans. Instrum. Meas.* **2025**, *74*, 9537413.

(32) Ferk, G.; Krajnc, P.; Hamler, A.; Mertelj, A.; Cebollada, F.; Drofenik, M.; Lisjak, D. Monolithic Magneto-Optical Nanocomposites of Barium Hexaferrite Platelets in PMMA. *Sci. Rep.* **2015**, *5*, 11395.

(33) Medle Rupnik, P.; Lisjak, D.; Čopič, M.; Mertelj, A. Ferromagnetic Liquid Crystals for Magnetic Field Visualisation. *Liq. Cryst.* **2015**, *42*, 1648−1688.

(34) Mur, M.; Sofi, J. A.; Kvasić, I.; Mertelj, A.; Lisjak, D.; Niranjan, V.; Muševič, I.; Dhara, S. Magnetic-Field Tuning of Whispering Gallery Mode Lasing from Ferromagnetic Nematic Liquid Crystal Microdroplets. *Opt. Express.* **2017**, *25*, 1073−1083.

(35) Al-Bustami, H.; Koplovitz, G.; Primc, D.; Yochelis, S.; Capua, E.; Porath, D.; Naaman, R.; Paltiel, Y. Single Nanoparticle Magnetic Spin Memristor. *Small* **2018**, *14*, 1801249.

(36) Koplovitz, G.; Primc, D.; Dor, O. B.; Yochelis, S.; Rotem, D.; Porath, D.; Paltiel, Y.; Paltiel, Y. Magnetic Nanoplatelet-Based Spin Memory Device Operating at Ambient Temperatures. *Adv. Mater.* **2017**, *29* (17), 1606748.

(37) Lisjak, D.; Ovtar, S. The Alignment of Barium Ferrite Nanoparticles from Their Suspensions in Electric and Magnetic Fields. *J. Phys. Chem. B* **2013**, *117*, 1644−1650.

(38) Goršak, T.; Jarc Jovičić, E.; Tratnjek, L.; Križaj, I.; Sepúlveda, B.; Nogués, J.; Erdani Kreft, M.; Petan, T.; Kralj, S.; Makovec, D. The Efficient Magneto-Mechanical Actuation of Cancer Cells Using a Very Low Concentration of Non-Interacting Ferrimagnetic Hexaferrite Nanoplatelets. *J. Colloid Interface Sci.* **2024**, *657*, 778−787.

(39) Hu, J.; Goršak, T.; Martín Rodríguez, E.; Calle, D.; Muñoz-Ortiz, T.; Jaque, D.; Fernández, N.; Cussó, L.; Rivero, F.; Aguilar Torres, R.; et al. Magnetic Nanoplatelets for High Contrast Cardiovascular Imaging by Magnetically Modulated Optical Coherence Tomography. *ChemPhotochem* **2019**, 3 (7), 529−539.

(40) Drofenik, M.; Kristl, M.; Žnidaršič, A.; Hanžel, D.; Lisjak, D. Hydrothermal Synthesis of Ba-Hexaferrite Nanoparticles. *J. Am. Ceram. Soc.* **2007**, *90*, 2057−2061.

(41) Perdew, J. P.; Burke, K.; Ernzerhof, M. Generalized Gradient Approximation Made Simple. *Phys. Rev. Lett.* **1996**, *77*, 3865−3868.

(42) van Setten, M. J.; Giantomassi, M.; Bousquet, E.; Verstraete, M. J.; Hamann, D. R.; Gonze, X.; Rignanese, G.-M. The PseudoDojo: Training and Grading a 85-Element Optimized Norm-Conserving Pseudopotential Table. *Comput. Phys. Commun.* **2018**, *226*, 39−54.

(43) Monkhorst, H. J.; Pack, J. D. Special Points for Brillouin-Zone Integrations. *Phys. Rev. B* **1976**, *13*, 5188−5192.

(44) Gorter, E. W. Saturation Magnetization of Some Ferrimagnetic Oxides with Hexagonal Crystal Structures. *Proc. IEE, Part B: Radio Electron. Eng.* **1957**, *104*, 255−260.

(45) Cococcioni, M.; de Gironcoli, S. Linear Response Approach to the Calculation of the Effective Interaction Parameters in the LDA+U Method. *Phys. Rev. B:Condens. Matter Mater. Phys.* **2005**, *71*, 035105.

(46) Timrov, I.; Marzari, N.; Cococcioni, M. Hubbard Parameters from Density-Functional Perturbation Theory. *Phys. Rev. B:Condens. Matter Mater. Phys.* **2018**, *98*, 085127.

(47) Giannozzi, P.; Baroni, S.; Bonini, N.; Calandra, M.; Car, R.; Cavazzoni, C.; Ceresoli, D.; Chiarotti, G. L.; Cococcioni, M.; Dabo, I.; Dal Corso, A.; de Gironcoli, S.; Fabris, S.; Fratesi, G.; Gebauer, R.; Gerstmann, U.; Gougoussis, C.; Kokalj, A.; Lazzeri, M.; Martin-Samos, F.; Marzari, N.; Mauri, F.; Mazzarello, R.; Paolini, S.; Pasquarello, A.; Paulatto, L.; Sbraccia, C.; Scandolo, S.; Sclauzero, G.; Seitsonen, A. P.; Smogunov, A.; Umari, P.; Wentzcovitch, R. M. QUANTUM ESPRESSO: A Modular and Open-Source Software Project for Quantum Simulations of Materials. *J. Phys.: Condens. Matter* **2009**, *21*, 395502.

(48) Giannozzi, P.; Andreussi, O.; Brumme, T.; Bunau, O.; Buongiorno Nardelli, M.; Calandra, M.; Car, R.; Cavazzoni, C.; Ceresoli, D.; Cococcioni, M.et al. Advanced Capabilities for Materials Modelling with Quantum ESPRESSO. *arXiv* **2017**, .

(49) Kokalj, A. XCrySDen—A New Program for Displaying Crystalline Structures and Electron Densities. *J. Mol. Graphics Modell.* **1999**, *17*, 176−179.

(50) Reuter, K.; Scheffler, M. First-Principles Atomistic Thermodynamics for Oxidation Catalysis: Surface Phase Diagrams and Catalytically Interesting Regions. *Phys. Rev. Lett.* **2003**, *90*, 046103.

(51) Drofenik, M.; Ban, I.; Ferk, G.; Makovec, D.; Žnidaršič, A.; Jagličić, Z.; Lisjak, D. The Concept of a Low-Temperature Synthesis for Superparamagnetic $BaFe_{12}O_{19}$ Particles. *J. Am. Ceram. Soc.* **2010**, *93*, 1602−1607.

(52) Miranda, L.; Sinclair, D. C.; Hernando, M.; Varela, A.; Wattiaux, A.; Boulahya, K.; Gonzalez-Calbet, J. M.; Parras, M. Mn-Rich $BaMn_{1-x}Fe_xO_{3-\delta}$ Perovskites Revisited: Structural, Magnetic, and Electrical Properties of Two New 6H0 Polytypes. *Chem. Mater.* **2009**, *21*, 5272−5283.

(53) Wakiya, K.; Sato, H.; Miyazaki, A.; Enoki, T.; Isobe, M.; Ueda, Y. Structure, Magnetism and Electrical Conductivity of a New Ternary Manganese Oxide: $BaMn_3O_6$. *J. Alloys Compd.* **2001**, *317−318*, 115−119.

(54) Dudziak, S.; Ryzynska, Z.; Bielan, Z.; Ryl, J.; Klimczuk, T.; Zielinska-Jurek, A. Pseudo-Superparamagnetic Behaviour of Barium Hexaferrite Particles. *RSC Adv.* **2020**, *10*, 18784−18796.

(55) Biesinger, M. C.; Payne, B. P.; Grosvenor, A. P.; Lau, L. W. M.; Gerson, A. R.; Smart, R. S. C. Resolving Surface Chemical States in XPS Analysis of First Row Transition Metals, Oxides and Hydroxides: Cr, Mn, Fe, Co and Ni. *Appl. Surf. Sci.* **2011**, *257*, 2717−2730.

(56) Drobež, K.; Popov, N.; Lisjak, D. Effect of the catechol structure on the functionalization and magnetic properties of barium hexaferrite nanoplatelets. *Nanoscale Adv.* **2025**, *7*, 4886−4896.

(57) Kaur, P.; Singh, S.; Kumar, V.; Tikoo, K. B.; Chudasama, B.; Kaushik, A.; Singhal, S. Interesting Makeover of Strontium Hexaferrites for Environmental Remediation from Excellent Photocatalysts to Outstanding Adsorbents via Inclusion of Mn^{3+} into the Lattice. *J. Alloys Compd.* **2019**, *791*, 508−521.

(58) Sharma, P.; Rocha, R. A.; Medeiros, S. N.; Hallouche, B.; Paesano, A. Structural and Magnetic Studies on Mechanosynthesized $BaFe_{12-x}Mn_xO_{19}$. *J. Magn. Magn. Mater.* **2007**, *316*, 29−33.

(59) Koch, C. T.*Determination Of Core Structure Periodicity And Point Defect Density Along Dislocations*; Ph.D. Thesis, Arizona State University: Tempe, AZ, 2002.

(60) Lazić, I.; Bosch, E. G. T.; Lazar, S.; Wirix, M.; Yücelen, E. Integrated Differential Phase Contrast (iDPC)—Direct Phase Imaging in STEM for Thin Samples. *Microsc. Microanal.* **2016**, *22*, 36−37.

(61) Aschauer, U.; Pfenninger, R.; Selbach, S. M.; Grande, T.; Spaldin, N. A. Strain-Controlled Oxygen Vacancy Formation and Ordering in $CaMnO_3$. *Phys. Rev. B* **2013**, *88*, 054111.

(62) Kim, H.; Zhang, J. Y.; Raghavan, S.; Stemmer, S. Direct Observation of Sr Vacancies in $SrTiO_3$ by Quantitative Scanning Transmission Electron Microscopy. *Phys. Rev. X* **2016**, *6*, 041063.

(63) Kreisel, J.; Lucazeau, G.; Vincent, H. Raman Spectra and Vibrational Analysis of $BaFe_{12}O_{19}$ Hexagonal Ferrite. *J. Solid State Chem.* **1998**, *137*, 127−137.

(64) Holtstam, D.; Hålenius, U. Nomenclature of the Magnetoplumbite Group. *Mineral. Mag.* **2020**, *84*, 376−380.

(65) Edström, K.; Ito, S.; Delaplane, R. G. The Magnetic Structure in K^+ β-Ferrite. *Phys. B* **2000**, *276−278*, 746−747.

(66) Ito, S.; Kurosawa, H.; Akashi, K.; Michiue, Y.; Watanabe, M. Crystal Structure and Electric Conductivity of K^+-β-Ferrite with Ideal Composition $KFe_{11}O_{17}$. *Solid State Ionics* **1996**, *86−88*, 745−750.

(67) Stergiou, A. C.; Litsardakis, G.; Samaras, D. Crystal Structure of Nonstoichiometric Mixed (Ba,K,Na) Hexagonal Ferrite $Ba_{0.71}Na_{0.64}K_{0.31}Fe_{10.55}Mg_{0.29}O_{17.30}$. *Solid State Ionics* **1998**, *109*, 55−64.

(68) Galuskin, E. V.; Galuskina, I. O.; Widmer, R.; Armbruster, T. First Natural Hexaferrite with Mixed β''-Ferrite (β-Alumina) and Magnetoplumbite Structure from Jabel Harmun, Palestinian Autonomy. *Eur. J. Mineral.* **2018**, *30*, 559−567.

(69) Mikheykin, A. S.; Zhukova, E. S.; Torgashev, V. I.; Razumnaya, A. G.; Yuzyuk, Y. I.; Gorshunov, B. P.; Prokhorov, A. S.; Sashin, A. E.; Bush, A. A.; Dressel, M. M Lattice anharmonicity and polar soft mode in ferrimagnetic M-type hexaferrite $BaFe_{12}O_{19}$ single crystal. *Eur. Phys. J. B* **2014**, *87*, 232.

(70) Chukalkin, Y. G.; Petrov, V. V.; Goshchitskii, B. N. Radiation Effects in Hexagonal Ferrite $BaFe_{12}O_{19}$. *Phys. Status Solidi A* **1981**, *67*, 421−426.

(71) Makovec, D.; Gyergyek, S.; Goršak, T.; Belec, B.; Lisjak, D. Evolution of the Microstructure during the Early Stages of Sintering Barium Hexaferrite Nanoplatelets. *J. Eur. Ceram. Soc.* **2019**, *39*, 4831−4841.